

NANOHYBRIDS COMPRISING REDUCED GRAPHENE OXIDE (GrO) AND POROUS Fe₂O₃ NANORODS HAVE BEEN PRODUCED AND SHOW REMARKABLE MICROWAVE ABSORPTION

*Nageshwar G, ** Dr. Kailas Narayan Sonune

*Research Scholar, **Research Supervisor

Faculty of Chemistry, OPJS University, Churu, Rajasthan

ABSTRACT

Exceptional physicochemical properties make nanocomposites (NCs) based on metal oxides and graphene derivatives appealing in environmental cleanup, optics, and cancer therapy. Tin oxide-reduced graphene oxide nanocomposites (SnO₂ rGO NCs) have potential environmental and biological applications, although little is known about them at this time. Examining SnO₂rGO NCs' photocatalytic activity and cancer-fighting potential was the focus of this study. Using a one-pot hydrothermal process, both pure SnO₂ NPs and SnO₂rGO NCs were produced. The synthesized samples were characterized using a wide range of techniques, including X-ray diffraction (XRD), transmission electron microscopy (TEM), scanning electron microscopy (SEM), X-ray photoelectron spectroscopy (XPS), Fourier transform infrared (FTIR), ultraviolet-visible spectrometry (UV-Vis), photoluminescence (PL), and Raman scattering microscopy. This study details the uniform chemical precipitation of Fe(OH)₃ and the concomitant reduction of Ag to produce a composite of Ag/Fe₂O₃ atop reduced graphene oxide (rGO) in a single hydrothermal reaction (I). Blending pure aqueous suspension of Hummers-synthesized graphene oxide (GO) with Fe(NO₃)₃·9H₂O, AgNO₃, urea, and polyethylene glycol (PEG 4000). An Ag/a-Fe₂O₃-rGO nanohybrid is formed when the combination is subjected to hydrothermal conditions. In this case PEG 4000 acts as both a surfactant and a reducing agent for Ag (I). In a room-temperature chemo selective reduction of aromatic nitro groups to the corresponding amines, the produced Ag/Fe₂O₃-rGO nanocomposite was utilized as a magnetically recoverable catalyst.

Keywords: SnO₂; rGO; nanocomposites; one-pot synthesis; characterization

INTRODUCTION

After lung cancer, hepatocellular carcinoma is the largest cause of cancer-related death worldwide. About 19 million new cases of cancer and about 10 million deaths from cancer were estimated by the World Health Organization (WHO) in 2020. Cancer can be treated in a number of ways, including surgical removal, radiation therapy, and chemotherapy. However, cancer treatment still faces significant challenges, including medication resistance and lack of selectivity. However, the release of environmental toxins from several factories threatens the health of the ecosystem. As a result, it is crucial to create a nanostructure with dual-use potential in the biological and environmental sectors. Silver nanoparticles (AgNPs) are just one type of metal nanoparticle that

has recently attracted attention for their potential uses in a variety of fields, including catalysis, biosensing, antibacterial activity, and biomedicine.

Applications of metal oxide nanoparticles (NPs) in cancer therapy and environmental cleanup have been demonstrated. Because of their one-of-a-kind physicochemical features, NPs of ZnO, TiO₂, WO₃, and In₂O₃ have been widely explored for applications including catalysis, cancer treatment, bacteria prevention, electronics, and photodegradation. Tin oxide (SnO₂) NPs were explored in depth for this purpose because they are an n-type semiconductor with a wide bandgap of 3.6 eV and offer a number of benefits for this application, including low cost, stability, rapid synthesis, and low toxicity. SnO₂ NPs, nanorods, and nanowires have all been synthesized using the hydrothermal technique. Previous research has demonstrated that SnO₂ NPs exhibit photocatalytic activity when exposed to either ultraviolet (UV) or visible light. The photocatalytic efficiency of these nanostructures, however, has a lot of room for development. Graphene is a single layer 2D nanocrystal made up of carbon atoms organized in a honeycomb lattice. The most well-known modifications of graphene are graphene oxide (GO) and reduced graphene oxide (rGO). Great surface area, high mechanical strength, outstanding optical quality, and the presence of functional groups on their surfaces are just a few of the reasons why GO and rGO are such promising materials for a wide range of applications.

Functional groups found in GO and rGO have piqued the interest of material scientists in their use as building blocks for nanocomposites with metal oxide NPs. Previous research has looked at how incorporating GO or rGO into metal oxide NPs can improve their physicochemical properties. In addition, GO offers a variety of benefits that boost the natural polymer's capabilities when used as a nanocomposite. Strong and biocompatible, for instance, are composites of natural polymer with GO (KGM/GO). Metal oxide NPs anchored on GO/rGO nanosheets were prepared using a variety of synthesis methods, including laser irradiation, gas-liquid interface contact, co-precipitation, and hydrothermal. The combined properties of these nanocomposites are greater than those of their component parts. When compared to pure ZnO NPs, ZnO-rGO nanocrystals (NCs) perform better in anticancer tests. The green manufacture of Argo NCs for photothermal therapy (PTT) of MCF7 cancer cells holds great promise for their use in nano biomedicine. A different study found that doping Fe₃O₄ NPs with rGO enhanced their photocatalytic activity.

The produced Pd nano catalyst reportedly showed excellent catalytic applicability for reducing extremely hazardous Cr(VI) and a wide variety of azo dyes. In light of the foregoing, we sought to increase the anticancer and photocatalytic activities of SnO₂ NPs by adding rGO. The one-pot hydrothermal approach was used to produce both pure SnO₂ NPs and SnO₂rGO NCs. The prepared samples' physicochemical properties were characterized via X-ray diffraction (XRD), field emission scanning electron microscopy (FE-SEM), field emission transmission electron microscopy (FE-TEM), X-ray photoelectron microscopy (XPS), Raman scattering microscopy (RSM), Fourier transmission infrared (FTIR) microscopy, ultraviolet-visible (UV-Vis) spectrometry (UV-Vis), and photo Under UV light, we compared the photocatalytic activity of SnO₂ NPs and SnO₂rGO NCs against methylene blue (MB) dye. Human liver cancer (HepG₂) and human lung cancer (H460) cells were used to test the samples for anticancer activity (A549).

LITERATURE REVIEW

Freddie Bray (2018) Using the GLOBOCAN 2018 estimates of cancer incidence and death issued by the International Agency for Research on Cancer, this article presents a status update on the worldwide burden of cancer with a particular emphasis on regional diversity across 20 world regions. This year, it is predicted that there would be 18.1 million new instances of cancer (17.0 million excluding nonmelanoma skin cancer) and 9.6 million cancer-related deaths. Lung cancer is the leading cause of cancer death among both sexes (18.4% of all cancer deaths), followed by breast cancer in women (11.6% of all cancer cases), prostate cancer (7.1%), and colorectal cancer (6.1%), and then stomach cancer (8.2% of all cancer deaths), and liver cancer (8.2% of all cancer deaths). Among men, lung cancer is the most common type and the primary cause of cancer death. This is followed by prostate and colorectal cancers (in terms of incidence) and liver and stomach cancers (for mortality). Breast cancer is the most prevalent malignancy in women and the main cause of cancer death, followed by colorectal and lung cancer (in terms of incidence) and vice versa (in terms of mortality); cervical cancer is ranked fourth for both. However, depending on economic development and related social and lifestyle factors, both the most commonly diagnosed cancer and the primary cause of cancer death significantly vary between countries and even within each country. Most low and middle-income nations lack access to high-quality cancer registry data, which is necessary for developing and enforcing evidence-based cancer control initiatives.

Maqsood Ahamed (2022) As a result of their unique and modifiable physicochemical properties, ZnO nanoparticles (NPs) have garnered a lot of interest for application in cancer therapy. Date palm (*Phoenix dactylifera* L.) fruit extract was used to prepare pure ZnO NPs, Molybdenum (Mo)-doped ZnO NPs, and Mo-ZnO/reduced graphene oxide nanocomposites (Mo-ZnO/RGO NCs) in a way that was simple, economical, and environmentally friendly. Two types of cancer cells were used to test the cytotoxic effects of green-synthesized NPs/NCs. Oxidative stress and apoptosis were investigated as possible mechanisms behind the anticancer effect of green produced NPs/NCs. X-ray diffraction (XRD), transmission electron microscopy (TEM), scanning electron microscopy (SEM), energy-dispersive X-ray spectroscopy (EDS), and photoluminescence (PL) validated the syntheses of pure ZnO NPs, Mo-ZnO NPs, and Mo-ZnO/RGO NCs (PL). In a dynamic light scattering (DLS) analysis, it was found that the colloidal stability of the greenly produced samples was exceptional. When compared to pure ZnO NPs, the anticancer activity of Mo-ZnO/RGO NCs was three times stronger in human colon (HCT116) and breast (MCF7) cancer cells. Mo-ZnO/RGO NCs mediated anticancer action via ROS, p53, and caspase-3. Mo-ZnO/RGO NCs were also much more cytocompatibility than pure ZnO NPs in human normal colon epithelial (NCM460) and normal breast epithelial (MCF10A) cells. Overall, the green mediated good synergism between ZnO, Mo, and RGO in green stabilized Mo-ZnO/RGO NCs led to increased anticancer performance and enhanced cytocompatibility. This research backed up the use of fruit-based, facile manufacturing of ZnO-based nanocomposites for cancer therapy, citing its high nutritional value.

Salvatore V. Giofrè (2022) Graphene quantum dots (GQDs), the next generation of the graphene family, are at the forefront of nanotechnology development due to their exceptional

physicochemical features. Hydrophilic functionalities found in GQDs make it possible for them to be dispersed in water, but they can also be a problem for reactions that typically take place in organic solvents, such as cycloaddition reactions. We looked into the 1,3-dipolar cycloaddition (1,3-DCA) interactions of C-methoxycarbonyl N-methyl nitrene 1a and C-diethoxy phosphoryl propylidene N-benzyl nitrene 1b with the surface of GQDs, yielding the isoxazolidine cycloadducts isox-GQDs 2a and isox-GQDs 2b. Using a natural deep eutectic solvent (NADES) made from the zwitterionic trimethyl glycine as the π -bond acceptor and glycolic acid as the hydrogen-bond donor, the reactions were carried out under mild and environmentally acceptable conditions. This study's findings show for the first time that it is possible to perform cycloaddition reactions directly to the π -cloud of the GQDs surface. It has been demonstrated that the high affinity of these green solvents with aromatic systems provides additional benefits when using DES for cycloaddition reactions on GQDs, beyond simply increasing the solubility of reactants.

Y. Liu, Liping Huang (2019) Easy and environmentally friendly biosynthesis of gold nanoparticles (AuNPs) is demonstrated. The AuNPs are prepared using an extract of Ginkgo biloba (*G. biloba*) leaf in the form of a bio-aqueous solution. Each Ginkgo biloba leaf serves as both a reducing agent and a stabilizing agent in the photochemical process. This method constitutes "green chemistry" because it eliminates the need for any chemicals that could cause harm to humans or the environment. A number of synthetic parameters, including reactant concentration, medium pH, reaction duration, and temperature, are adjusted, leading to the synthesis of AuNPs of consistent size. Scanning electron microscopy (SEM), high resolution-transmission electron microscopy (HRTEM), X-ray diffraction (XRD), energy dispersive X-ray (EDX) spectroscopy, fringe spacing and selected area diffraction (SEAD) pattern, and dynamic light scattering (DLS) are just some of the analytical techniques used to characterize AuNPs. The AuNPs are spherical in shape and exhibit a cubic structure, with an average size of 18.95 \pm 5.95 nm. The azo-dyes can be catalytically decolorized by adding sodium borohydride to the produced AuNPs, and the results are promising (Nabha 4). The detection limit for Cr(VI) using AuNPs was found to be between 0.1 and 0.8 M, demonstrating their excellent sensitivity. Researchers hope that their findings will encourage them to continue exploring the potential of metal nanoparticles in the fight against pollution in the natural world.

Nand K. Singh (2022) The cytotoxic and antioxidant activity of ZnO NPs (zinc oxide nanoparticles) green produced from *Senna occidentalis* leaf extract was evaluated in this study using the colon cancer SW480 cell line. Results UV-Vis spectroscopy, X-ray diffraction, Particle size analysis, Fourier transform infrared spectroscopy, Field emission scanning electron microscopy, Energy-dispersive X-ray spectroscopy, and atomic force microscopy were all used to characterize zinc oxide nanoparticles. The ZnO NPs were 20-50 nm in size, approximately cuboidal in shape, and irregular in shape, as revealed by the PSA, XRD, and AFM. Human colon cancer cell line (SW480) was used in an MTT and neutral red absorption assay to test the anticancer efficacy of the produced ZnO nanoparticles. After being exposed to ZnO NPs at concentrations ranging from 20 to 100 g/ml for 2 hours, SW480 colon cancer cells were tested for viability. ZnO NPs were found to promote membrane leakage and decrease cell viability in SW480 cells in a concentration-dependent manner, with a 50% reduction in cell viability being observed

at 100 g/ml. Conclusion Zinc oxide nanoparticles have demonstrated anticancer efficacy against colon cancer cell lines, suggesting their potential utility as an anticancer therapy (SW480).

METHOD

Materials and physical measurements

Sigma Aldrich was used to acquire the graphite powder, ferric nitrate, and silver nitrate used in this experiment. Merck India Ltd. was contacted for the acquisition of urea and PEG 4000. Throughout the experiment, double-distilled water was used. Using a Bruker 3000 Hyperion Microscope equipped with a Vertex 80 FT-IR system, an FT-IR spectra of KBr was acquired. thermal analyzer, TGA was conducted in air at a flow rate of 20 mL/min and a heating rate of 10 C/min. Powder X-ray diffraction measurements were taken on a Bruker AXS D8-Advance instrument using Cu-Ka radiation and a scan speed of 2 /min. Images were taken with a JEOL, JEM2100 transmission electron microscope. A few drops of the powdered sample were disseminated in ethanol using sonication, and then the TEM grids were prepared by drying the dispersion in air. By using a Micromeritics ASAP 2010 surface area and porosity analyzer, nitrogen adsorption-desorption isotherms may be determined. At 300 K, the material's magnetic properties were analyzed with a Lakeshore VSM 7410.

Synthesis of graphene oxide

The modified Hummers technique was used to oxidize graphite powder (GP). Specifically, in a 250 mL round bottomed flask (RB), concentrated H₃PO₄ and concentrated H₂SO₄ were combined, and then graphite powder was added. The RB was placed in a water bath prepared to 50 degrees Celsius, and magnetic stirring was continued for a further 6 hours while the KMnO₄ was slowly added. After this, diluted H₂O₂ was continuously added to the solution until no bubbles formed and the solution had turned from black to purple and then bright yellow. Another three hours were spent stirring the mixture. After cooling the solid product to room temperature, it was separated using a centrifuge. Graphene oxide was obtained when the product was rinsed with 5% HCl, ethanol, and deionized water. Ultrasound was used to remediate the collected silt, which was then dissolved in alcohol. After drying the sample at 90 C for 24 hours, its mass was measured to determine the graphene oxide concentration.

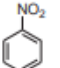
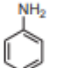
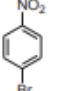
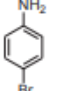
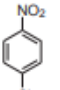
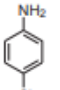
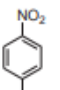
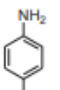
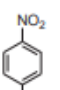
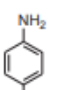
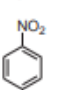
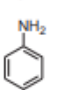
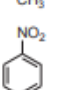
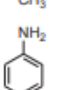
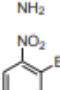
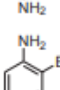
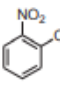
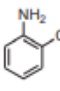
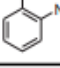
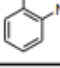
Synthesis of Ag/a-Fe₂O₃-rGO nanocomposite

To 20 mL of a 1.8 mg mL⁻¹ GO aqueous solution, 0.80 g of Fe (NO₃)₃·9H₂O (2 mmol) and 0.084 g of AgNO₃ (0.5 mmol) were added while stirring. The aforementioned mixture was sonicated for 15 minutes at 25 C after which 1.08 g of urea (0.018 M) and 2 g of PEG 4000 (0.5 mmol) were added. After 15 minutes of sonication, the resultant solution was diluted with around 80 mL of deionized water, placed in a 100 mL Teflon-lined stainless-steel autoclave, and cooked at 180 C in an electric oven for 8 hours. After cooling the black product to ambient temperature, it was cleaned multiple times in deionized water and ethanol. At the end, the product was dried in a

vacuum oven for three hours at fifty degrees Celsius. To provide a point of reference, the same conditions were used to synthesize a nano Ag/a-Fe₂O₃ material devoid of GO for comparison.

Procedure for the Room Temperature Reduction of Nitroarenes (Section 2.4) An aqueous suspension of 50 mg of freshly manufactured nanoparticles catalysts (Ag/a-Fe₂O₃-rGO) is typically agitated at room temperature for about 5 minutes while 1.0 mmol of aromatic nitro compound is gently added. The reaction mixture was further agitated after 0.2 mL of hydrazine monohydrate was added. The recommended stirring time (Table 1) was adhered to in order to ensure a full conversion. The reaction was followed using thin-layer chromatography. Once the reaction was complete, the catalyst was removed using a magnetic separator, and the product was extracted using ethyl acetate (3-5 mL). Finally, the solvent was evaporated under vacuum while the organic layer was dried over anhydrous Na₂SO₄. The ¹H NMR was used to characterize all of the final compounds (400 MHz with TMS as the standard).

Table 1. Reduction of nitroarenes in presence of Ag/a-Fe₂O₃-rGO catalyst.

| Entry | Substrate | Product | Time (min) | Yield (%) | Selectivity (%) |
|-------|---|---|------------|-----------|-----------------|
| 1 |  |  | 30 | 98 | >99 |
| 2 |  |  | 25 | 98 | >99 |
| 3 |  |  | 45 | 97 | >99 |
| 4 |  |  | 30 | 95 | >99 |
| 5 |  |  | 20 | 98 | >99 |
| 6 |  |  | 60 | 95 | >99 |
| 7 |  |  | 30 | 99 | >99 |
| 8 |  |  | 45 | 92 | >99 |
| 9 |  |  | 40 | 95 | >99 |
| 10 |  |  | 90 | 92 | >99 |

RESULTS AND DISCUSSION

Hydrothermal heating of a ferric hydroxide ($\text{Fe}(\text{OH})_3$) precursor prepared by homogenous chemical precipitation and concomitant reduction of $\text{Ag}(\text{I})$ has resulted in the synthesis of a composite of $\text{Ag}/\text{Fe}_2\text{O}_3$ anchored on rGO (Scheme 1). The hydroxylation process in this case relied on the usage of urea. At the temperature used in the experiment, urea decomposes into ammonia and carbon dioxide. Ammonium (NH_4) and hydroxide (OH) ions are formed when NH_3 is dissolved in water. In this case, the pH of the solution increases uniformly until the solubility limit due to the production of hydroxide anions by urea's hydration. After that, the free OH ions join with the Fe_3^+ ions to create $\text{Fe}(\text{OH})_3$. Here, it's worth noting that polyethylene glycol (PEG) with a homogeneous and ordered chain structure can function as a highly beneficial surfactant to regulate the dimensions and shape of nanomaterials.

The primary benefit of utilizing urea is that no additional reducing agent, like sodium borohydride, aluminum hydride, hydrohalic acid, hydrazine, etc., is needed for the reduction of GO to rGO. To accomplish this synthesis, urea was used not only as a hydroxylating agent, but also as a reducing agent for GO. Here, PEG 4000 acts as a reducing agent for AgNO_3 and a surfactant to regulate the particle size and size distribution of the nanoparticles. In situ reduction of the pure GO during a hydrothermal treatment at 180°C for 8 h results in the growth of $\text{Ag}/\text{a-Fe}_2\text{O}_3$ nanoparticles on the surfaces of the reduced graphene oxide nanosheets. The primary benefit of this procedure is that nucleation may take place consistently across the solution because to the uniform rise in pH, which eliminates the possibility of excessive local supersaturation.

CATALYST CHARACTERIZATION

XRD analysis of the catalyst

It was necessary to record the powder XRD pattern so that the phases displayed by the produced material could be identified. The powder XRD pattern of the produced $\text{Ag}/\text{a-Fe}_2\text{O}_3$ -rGO nanocomposite is presented in Fig. 1. The shape of the diffraction peaks is consistent with that of $\text{a-Fe}_2\text{O}_3$ (JCPDS File no. 87e1166). $\text{a-Fe}_2\text{O}_3$ has a close-packed oxygen lattice with a rhombohedral centered hexagonal structure of the corundum type, and two-thirds of the octahedral sites are occupied by Fe (III) ions. Diffraction peaks at $2\theta = 38.19$ and 44.46 correspond to the (111), and (200) planes of face-centered cubic Ag, respectively (JCPDS File no. 87-0720). This is evidence that pure $\text{Ag}/\text{a-Fe}_2\text{O}_3$ nanoparticles have formed. An additional diffraction peak, at 25.5 , was observed for the $\text{Ag}/\text{a-Fe}_2\text{O}_3$ -rGO nanocomposite, and it was assigned to the (002) plane of rGO. Debye-Scherrer equation was used to calculate the average crystallite size of the synthesized $\text{Ag}/\text{a-Fe}_2\text{O}_3$ -rGO nanocomposite: $d = \frac{0.94}{\lambda} \frac{1}{b \cos \theta}$, where d is the average crystallite size, λ is the wavelength of Cu-K α radiation, b is the full width at half maximum (FWHM) of the highest intensity diffraction peak, θ is the Bragg diffraction angle. The synthesized $\text{Ag}/\text{a-Fe}_2\text{O}_3$ -rGO nanocomposite has an average crystallite size of 25.1 nm.

TEM and EDS analysis of the catalyst

See Figure 1 for a transmission electron micrograph of the synthesized Ag/a-Fe₂O₃-rGO nanocomposite. The a-Fe₂O₃ and Ag nanoparticles are evenly dispersed throughout the rGO sheets, as observed in the TEM image. Figure 1 displays a Fe₂O₃ particles with a diameter of 10e35 nm and Ag NPs with a diameter of 2e5 nm. As seen in Fig. 1 of the ESI, Ag nanoparticles interact strongly with a-Fe₂O₃ nanoparticles. It was determined that the (110) plane of a-Fe₂O₃ and the (111) plane of metallic Ag separated the lattice fringes by 0.251 and 0.234 nm, respectively. Since the ED pattern was polycrystalline, the material must be of that type. Ag/a-Fe₂O₃-rGO nanocomposite production was confirmed by the presence of Fe, C, Ag, and O in the EDS signal (Fig. 1).

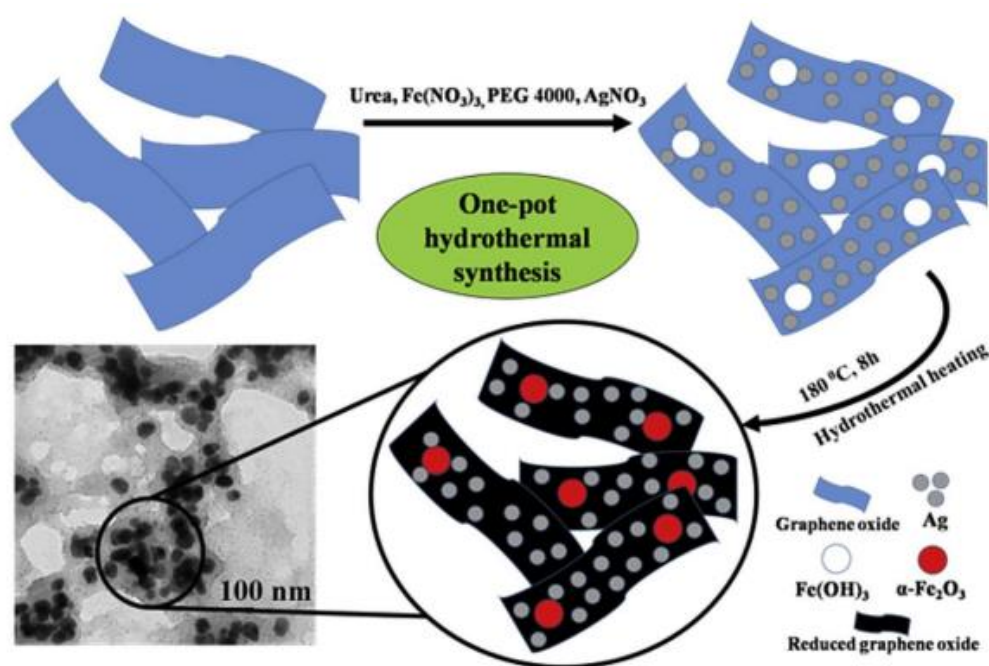


Figure 1. Synthesis of Ag/a-Fe₂O₃-rGO nanocomposite.

Raman spectra of the catalyst

GO and Ag/a-Fe₂O₃-rGO nanocomposite SERS signals are displayed in the 1000e1800 cm⁻¹ range in Fig. 2. The materials displayed two distinct peaks, one at 1352 cm⁻¹ (the defect (D) peak) and the other at 1590 cm⁻¹ (the graphite (G) peak). The values agree with those reported in the literature. The degree of disorder in a material is revealed by calculating the intensity ratio (ID/IG) of peaks in the D and G bands. GO and Ag/a-Fe₂O₃-rGO Ion-Diffusion/Ion-Gelation Spectroscopy nanocomposite, with the former being 0.826 and the latter being 1.001. An improved ID/IG ratio of Ag/a-Fe₂O₃-rGO was observed after the synthesis process, which was attributed to the transformation of GO into rGO.

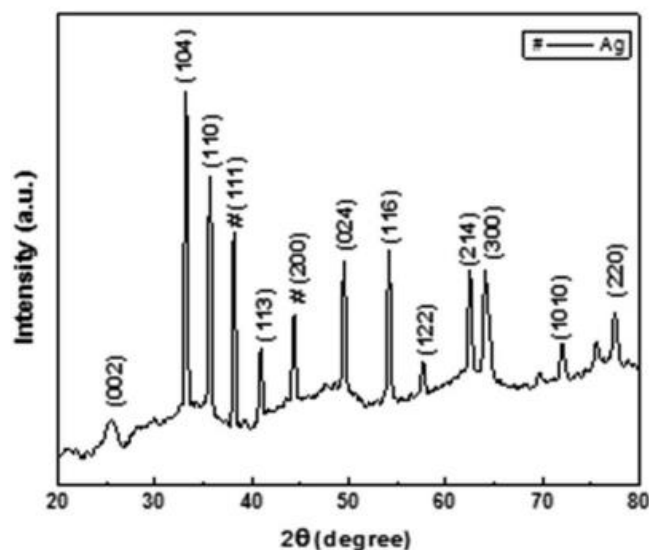


Figure 2. Powder XRD pattern of Ag/a-Fe₂O₃-rGO nanocomposite.

TGA of the catalyst

displays the TGA curves of GO and an Ag/a- Fe₂O₃-rGO nanocomposite. A maximum mass loss of 65% in the temperature range of 170–525 C can be attributed to the pyrolysis of the labile oxygen-containing groups in the forms of CO, CO₂, and steam, with a mass loss of 5% at about 100–170 C attributable to the removal of water molecules trapped inside the GO. After being heated to 800 degrees Celsius at a rate of 10 degrees per minute, Ag/a- Fe₂O₃- rGO lost just 17% of its initial weight. This decrease in mass is proportional to the elimination of the oxygen-containing groups in the rGO that had previously been present in the Ag/a- Fe₂O₃-rGO.

N₂ adsorption-desorption isotherm analysis of the catalyst

Ag/a- Fe₂O₃-rGO nanocomposite exhibits type IV characteristics in its N₂ adsorption-desorption isotherm (Fig. 3), with type H3 hysteresis loop associated with aggregation of plate-like particles creating slit-like pores. The BET specific surface area of the material was 772.65 m²/g, and its pore volume was 1.47 cm³/g. Most pores fall into the 5-20 nm range, as seen in the inset of Fig. 3, according to the Barrett Joyner Halina (BJH) pore size distribution. Examining the catalyst with a VSM Using a magnetic field that varied from 20,000 to 20,000 gauss (G), a measurement of the magnetic hysteresis of Ag/a- Fe₂O₃-rGO nanocomposite (Fig. 3) was made at 300 K. The remnant magnetization (M_r) was 15.13 emu g⁻¹ and the coercivity (H_c) was 572.03 G, indicating ferromagnetic behavior in the magnetic hysteresis loops. Saturation magnetization of Ag/a- Fe₂O₃-rGO catalyst is 57.2 emu g⁻¹. The saturation magnetization value and hysteresis loop shape both strongly suggest that the nanocomposite possesses ferromagnetic properties.

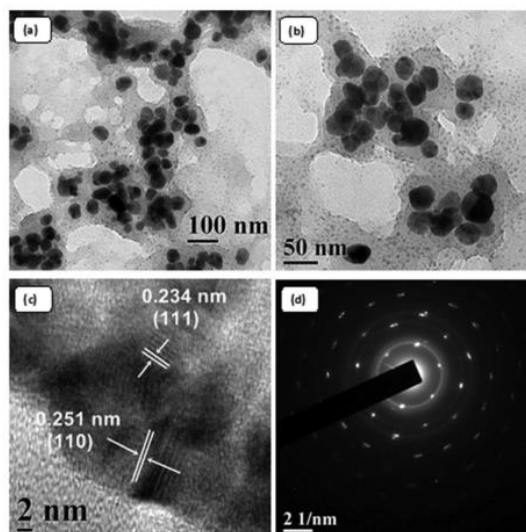
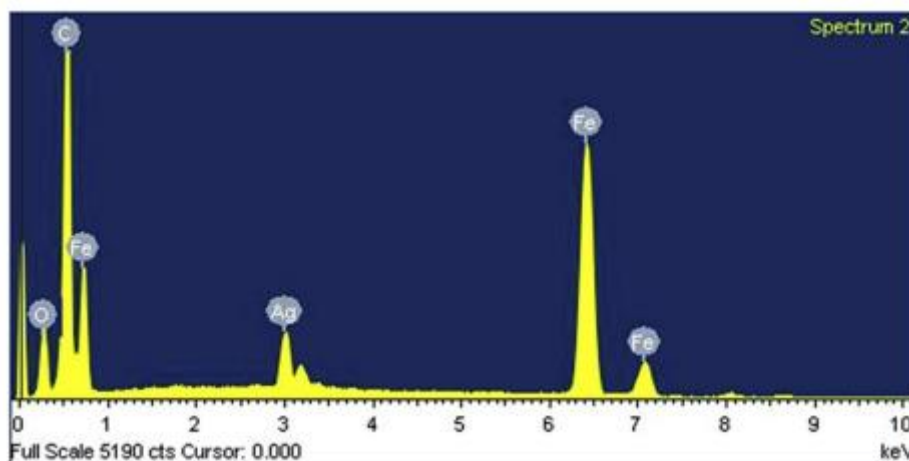


Figure 3. (a, b) TEM images (c) HRTEM image and (d) ED pattern of Ag/a-Fe₂O₃-rGO nanocomposite.

Catalytic activity of Ag/a-Fe₂O₃-rGO nanocomposite for reduction of nitroarenes using hydrazine monohydrate at room temperature.

After the nanocomposite had been synthesized and fully characterized, we tested its catalytic activity by subjecting it to the hydrazine hydrate-catalyzed reduction of nitroarenes to aromatic amines. The reaction factors, such as the solvent and the amount of catalyst, were tuned to get the greatest results. Specifically, nitrobenzene was selected as a representative substrate for this study. Each solvent—acetonitrile, dichloromethane, toluene, and water—was used in the experiment. The optimization analyses clearly show that water is the optimal solvent for the current catalytic system. Substrate, reducing agent, and catalyst mole ratios were also investigated in this process (Table 1). After a lengthy period of time, the product yield from a "blank run" in which the catalyst was not used was extremely low.



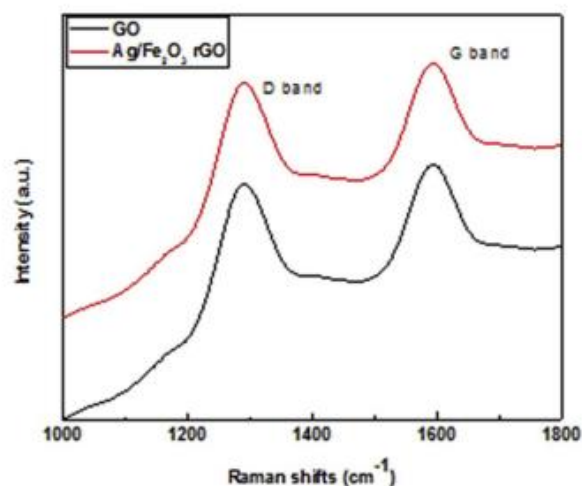


Figure 4. Raman spectra of GO and Ag/a-Fe₂O₃-rGO nanocomposite.

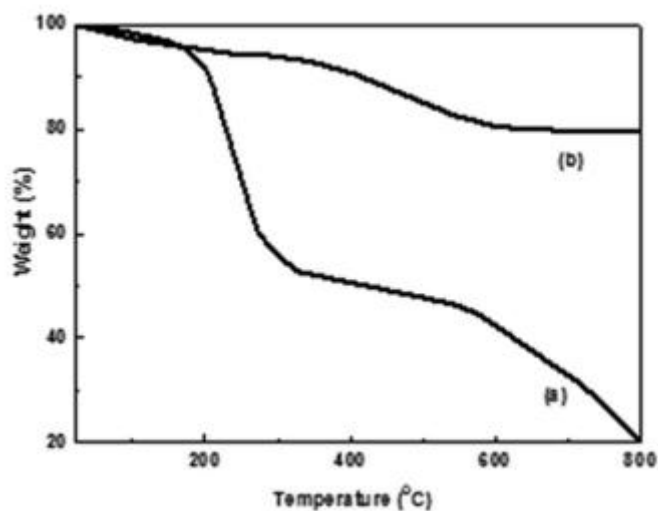


Figure. 5. TGA curve of (a) GO and (b) Ag/a-Fe₂O₃-rGO nanocomposite

The optimal conditions are 50 mg of catalyst and a substrate-to-reducing agent ratio of 1:4. The yield did not noticeably improve after adding more than four equivalents of reducing agent. This demonstrates the catalyst's versatility. Not surprisingly, nitroarenes with both electron-withdrawing and electron-donating functional groups provided high yields. Melting point measurements and infrared spectroscopy were used to describe each product. Independently, both Ag NPs and a Fe₂O₃ NPs display catalytic activity, albeit at a much lower efficiency compared to the nanocomposite, when used as catalyst for the reduction of nitroarenes to aromatic amines, as we have shown in our described techniques. We subsequently combined Ag NPs and a-Fe₂O₃ NPs at room temperature and employed this mixture as catalysts for reduction of nitroarenes, but the product yield did not increase.

Although the catalytic performance of Ag/a- Fe_2O_3 (Ag supported a- Fe_2O_3) was enhanced after synthesis and usage as catalysts, it was still not on par with that of the Ag/a- Fe_2O_3 -rGO nanocomposite. This strongly suggests that the catalytic effect on nitroarenes reduction is much lower for Ag NPs and a- Fe_2O_3 NRs when used alone, for a simple random mixture of these components, and for Ag/a- Fe_2O_3 . To sum up, rGO's support function in Ag/a Fe_2O_3 -rGO is crucial to the composite catalyst's efficiency gains. Table 2 provides a summary of the differences between the present catalyst and some of the previously described catalytic techniques for reducing nitroarenes to aromatic amines. After comparing to other catalytic reductions of aromatic nitroarenes to amines, it is clear that the one described above is the most effective. The present catalyst's added benefit is that it may be easily recovered and recycled.

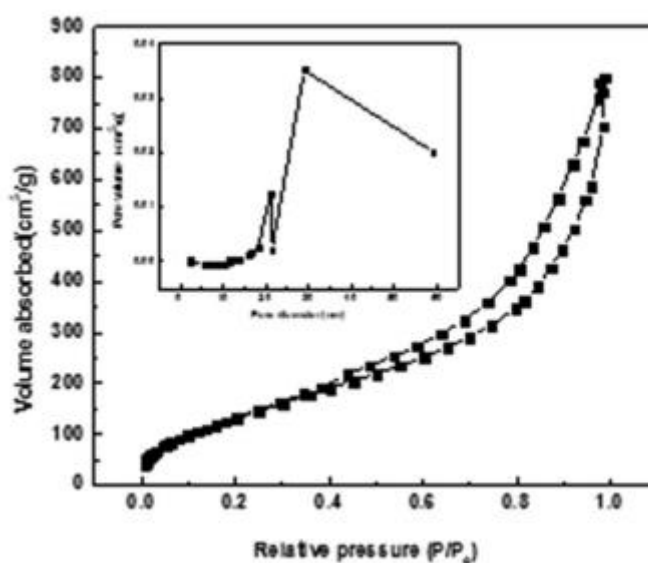


Figure. 6. (a, b) N_2 adsorption-desorption isotherms of Ag/a- Fe_2O_3 -rGO nanocomposite

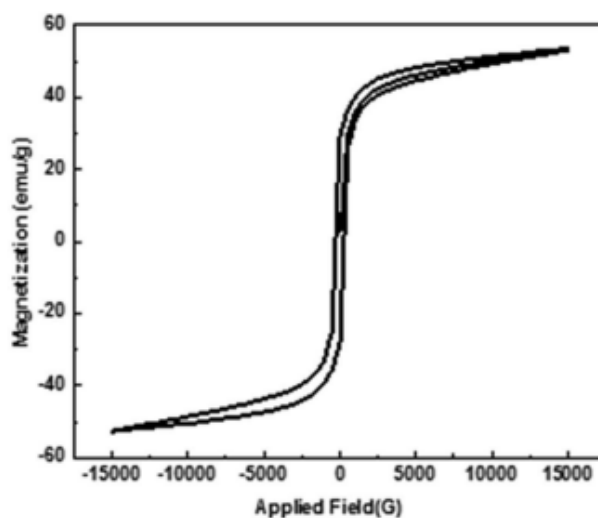


Figure. 7. Room temperature magnetization hysteresis loop of Ag/a- Fe_2O_3 -rGO nanocomposite.

Table 2 Comparison of the literature reported catalyst with the present catalyst

| Entry | Catalyst | Solvent | Temp °C | Time (min) | Yield/conversion (%) |
|-------|---|--|---------|------------|----------------------|
| 1 | Ni NPs | Water | rt | 75 | 99 conversion |
| 2 | Co NPs | Water | rt | 300 | 50 conversion |
| 3 | Au/TiO ₂ | EtOH | rt | 180 | 99 conversion |
| 4 | Ni-Fe ₃ O ₄ | Glycerol | 80 | 180 | 94 yield |
| 5 | Au-Fe ₃ O ₄ | EtOH | rt | 10 | GC yield 99 |
| 6 | Rh-Fe ₃ O ₄ | EtOH | 80 | 60 | 99 yield |
| 7 | Pd-Fe ₃ O ₄ | EtOH | rt | 60 | 90 yield |
| 8 | Fe ₃ O ₄ @SiO ₂ /EP.EN.EG@Cu | Water | rt | 15 | 85 yield |
| 9 | Reduced graphene oxide | N ₂ H ₄ ·H ₂ O/H ₂ O | 30 | 2880 | 97 yield |
| 10 | Ag/a-Fe ₂ O ₃ -rGO | Water | rt | 30 | 98 yield |

Recyclability of the catalyst

After the reaction was finished, the solid catalyst was magnetically removed from the reaction mixture, cleaned completely with acetone, and put through repeated cycles to test how well the recycled catalyst worked. In order to convert nitroarenes into aromatic amines, the same catalyst was utilized for the reduction reaction a second time. There was no discernible decrease in the recovered catalyst's activity after 5 iterations. A comparison of the fresh and used catalysts using TEM revealed that they were about the same size and shape. The leaching test was conducted according to the method described in. After 15 minutes, the catalyst was magnetically removed to ensure that no Ag particles were leached into the process. The 15-minute yield was recorded as a significant milestone. We tried running the reaction without the catalyst for a further 15 minutes but saw no improvement in yield. Given that Ag is one of the composite's catalytically active components, any leaching of Ag NPs would have resulted in a boost in yield. It follows that the Ag NPs are not washing away from the Ag/a-Fe₂O₃-rGO catalyst during the process.

CONCLUSIONS

In conclusion, a unique one-pot hydrothermal method was used to successfully synthesize SnO₂ NPs and SnO₂rGO NCs. The average crystallite size of the SnO₂ NPs was found to be smaller after rGO doping, as evidenced by XRD measurements. Based on HRTEM and SEM analysis, we know that the SnO₂ NPs serve as strong anchors for the rGO sheets, and that both SnO₂ and rGO are distributed equally throughout the SnO₂rGO NCs, resulting in distortion-free high-quality lattice fringes. The XPS and EDX results verified the SnO₂rGO NCs' chemical identity and elemental make-up. Based on optical measurements, it appeared that the SnO₂rGO NCs had a somewhat smaller bandgap energy than the pure SnO₂ NPs. The one-pot hydrothermal approach has been used successfully to produce an Ag/a-Fe₂O₃-rGO nanocomposite. Urea's hydroxylating activity and PEG 4000's dual function as surfactant and reducing agent are key to the synthesis's success. Recyclable catalytic reduction of a variety of aromatic nitroarenes to amines is facilitated by this new nanocomposite, Ag/a-Fe₂O₃-rGO. No prior use of a nanocomposite containing rGO for the conversion of nitroarenes to amines has been found to our knowledge. High yields, no need for homogenous catalysts, quick work-up, and separation and recycling of the catalyst are just a few of the benefits of this catalytic approach. The catalyst's genuine heterogeneity is demonstrated by the fact that its performance is essentially unchanged after five reuse cycles.

REFERENCES

1. Bray F, Ferlay J, Soerjomataram I, Siegel RL, Torre LA, Jemal A. Global cancer statistics 2018: GLOBOCAN estimates of incidence and mortality worldwide for 36 cancers in 185 countries. *CA Cancer J Clin.* 2018 Nov;68(6):394-424. doi: 10.3322/caac.21492. Epub 2018 Sep 12. Erratum in: *CA Cancer J Clin.* 2020 Jul;70(4):313. PMID: 30207593.
2. Ahamed, M.; Akhtar, M.J.; Khan, M.A.M.; Alhadlaq, H.A. Enhanced anticancer performance of eco-friendly-prepared Mo-ZnO/RGO nanocomposites: Role of oxidative stress and apoptosis. *ACS Omega* 2022, 7, 7103–7115. <https://doi.org/10.1021/acsomega.1c06789>.
3. Giofrè, S.V.; Tiecco, M.; Celesti, C.; Patanè, S.; Triolo, C.; Gulino, A.; Spitaleri, L.; Scalese, S.; Scuderi, M.; Iannazzo, D. Eco-friendly 1,3-dipolar cycloaddition reactions on graphene quantum dots in natural deep eutectic solvent. *Nanomaterials* 2020, 10, 2549. <https://doi.org/10.3390/nano10122549>.
4. Liu, Yinan et al. “Gold Nanoparticles Biosynthesized Using Ginkgo biloba Leaf Aqueous Extract for the Decolorization of Azo-Dyes and Fluorescent Detection of Cr(VI).” *Journal of Cluster Science* 31 (2019): 549-560.
5. Singh, M.P.; Sirohi, P.; Afzal, S. Biosynthesis zinc oxide nanoparticles using senna occidentalis leaf extract and evaluation of their cytotoxic effect on SW480 colon cancer cell line. *Res. Square* 2022, 1–20. <https://doi.org/10.21203/rs.3.rs-1215740/v1>.
6. Wang, Y. M., Li, T. X., Zhao, L. F., Hu, Z. W. & Gu, Y. J. Research progress on nanostructured radar absorbing materials. *Energy Power Eng.* 3, 580–584 (2011).
7. Qin, F. & Peng, H. X. Ferromagnetic microwires enabled multifunctional composite materials. *Prog. Mater. Sci.* 58, 183–259 (2013).
8. Saini, P. et al. High permittivity polyaniline-barium titanate nanocomposites with excellent electromagnetic interference shielding response. *Nanoscale* 5, 4330–4336 (2013).
9. Sun, G. B., Dong, B. X., Cao, M. H., Wei, B. Q. & Hu, C. W. Hierarchical dendrite-like magnetic materials of Fe₃O₄, γ -Fe₂O₃, and Fe with high performance of microwave absorption. *Chem. Mater.* 23, 1587–1593 (2011).
10. Qi, X. S. et al. Heteronanostructured Co@carbon nanotubes-graphene ternary hybrids: synthesis, electromagnetic and excellent microwave absorption properties. *Sci. Rep.* 6, 37972 (2016).
11. Zhao, B., Shao, G., Fan, B. B., Zhao, W. Y. & Zhang, R. Investigation of The electromagnetic absorption properties of Ni@TiO₂ and Ni@SiO₂ composite microspheres with core-shell structure. *Phys. Chem. Chem. Phys.* 17, 2531–2539 (2015).

- 12.** Ren, Y. J. et al. Tree-dimensional SiO₂@Fe₃O₄ core/shell nanorod array/graphene architecture: synthesis and electromagnetic absorption properties. *Nanoscale* 5, 12296–12303 (2013).
- 13.** Singh, V. K. et al. Microwave absorbing properties of a thermally reduced graphene oxide/nitrile butadiene rubber composite. *Carbon* 50, 2202–2208 (2012).
- 14.** Saini, P., Choudhary, V., Vijayan, N. & Kotnala, R. K. Improved electromagnetic interference shielding response of poly(aniline)- coated fabrics containing dielectric and magnetic nanoparticles. *J. Phys. Chem. C* 116, 13403–13412 (2012).
- 15.** Sun, Y. et al. Constructing two-, zero-, and one-dimensional integrated nanostructures: an effective strategy for high microwave absorption performance. *ACS Appl. Mater. Interfaces* 8, (31878–31886 (2016)).